Proceedings of the ASME 2011 International Mechanical Engineering Congress & Exposition
IMECE2011
November 11-17, 2011, Denver, Colorado, USA

IMECE2011-64005

FOUR-FIN BIO-INSPIRED UUV: MODELING AND CONTROL SOLUTIONS

Jason D. Geder
Laboratory for Computational Physics and Fluid Dynamics,
U.S. Naval Research Laboratory
Washington, DC, USA

Ravi Ramamurti
Laboratory for Computational Physics and Fluid Dynamics,
U.S. Naval Research Laboratory
Washington, DC, USA

John Palmisano
Center for Biomolecular Science and Engineering,
U.S. Naval Research Laboratory
Washington, DC, USA

Marius Pruessner
Center for Biomolecular Science and Engineering,
U.S. Naval Research Laboratory
Washington, DC, USA

Banahalli Ratna
Center for Biomolecular Science and Engineering,
U.S. Naval Research Laboratory
Washington, DC, USA

William C. Sandberg
Modeling and Analysis Division,
Science Applications International Corporation
McLean, VA, USA

ABSTRACT

This paper describes the modeling and control development of a bio-inspired unmanned underwater vehicle (UUV) propelled by four pectoral fins. Based on both computational fluid dynamics (CFD) and experimental fin data, we develop a UUV model that focuses on an accurate representation of the fin-generated forces. Models of these forces span a range of controllable fin parameters, as well as take into account leading-trailing fin interactions and free stream flow speeds. The vehicle model is validated by comparing open-loop simulated responses with experimentally measured responses to identical fin inputs. Closed-loop control algorithms, which command changes in fin kinematics, are tested on the vehicle. Comparison of experimental and simulation results for various maneuvers validates the fin and vehicle models, and demonstrates the precise maneuvering capabilities enabled by the actively controlled curvature pectoral fins.

INTRODUCTION

Current unmanned underwater vehicles excel at many critical tasks including deeply submerged and high-endurance operations, performing high-speed and large-radius maneuvers. However, the traditional propeller-driven vehicles performing these missions have not demonstrated the same levels of operational success in cluttered, near-shore environments where precise positioning and small-radius maneuvers are required in the presence of waves and alternating currents. Researchers have therefore studied the fin force production mechanisms employed by various fish species in their attempts to understand how these organisms achieve high levels of controllability in difficult environments [1]. Within fish swimming, articulation of the pectoral fins has been shown to produce forces and moments ideal for high-maneuverability in low-speed and hovering operations [2]. Several investigators have developed and adapted passively deforming robotic pectoral fins onto UUVs [3][4][5][6], whereas others have pursued the development of active control deformation pectoral fins [7][8][9].

In our previous work, we concluded that active control over the curvature of the robotic pectoral fins was necessary to achieve precise low-speed maneuverability of UUVs in highly time-varying external force environments, and others have come to similar conclusions about the use of fish-like fins [10][11]. Design, construction, and testing of such a fin on a two-fin vehicle have demonstrated the success of this strategy in achieving the force production and vehicle maneuvering capabilities necessary for operation in these challenging environments [8][12][13][14].

This paper details the subsequent development of a four-fin vehicle (Figure 1) which has more payload, greater top speed, and tighter turning capability than our two-fin active curvature-control technology demonstration vehicle. The modeling of this four-fin vehicle is described with particular emphasis on the fin models. Using our previous studies of fin force production

[8][15], the forces generated by the current flapping fins are determined both experimentally and computationally showing the effects various parameters have on fin force output. The most important of these parameters – controllable fin kinematics, leading-trailing fin fluid interaction, and free stream fluid velocity – are modeled to produce an accurate representation of fin force output for use in evaluating the vehicle control system.

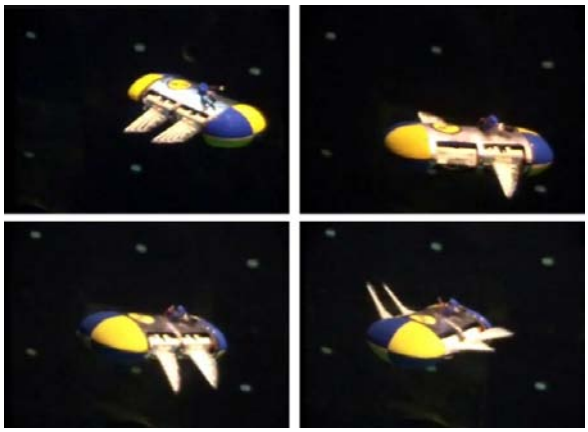

Fig. 1: Four-fin vehicle operating in Naval Research Lab test facility

Accuracy of the four-fin dynamics model is validated experimentally by measuring open-loop response of vehicle forward motion and heading to user specified fin kinematics. Further, open-loop performance comparisons of the four-fin vehicle to the two-fin vehicle show improvement in performance as a result of the new vehicle design. Finally, the modeling of the closed-loop controller for vehicle heading is validated through comparison of simulation and experimental results.

VEHICLE DESIGN AND MODEL

The Four-Fin Vehicle

Following the development of an actively controlled curvature robotic fin [8], initial testing was performed on a dynamic vehicle platform specifically designed to demonstrate the fin force production and control capability using two of these fins [14]. The payload volume was limited to accommodate only basic processing and sensing hardware needed to maintain stability and heading. The test results for this two-fin vehicle demonstrated that the fins were capable of propelling the vessel at the design speed. However, this vehicle had restricted options for sensor payload and did not have the fore-aft force production capability needed for heave-pitch control. Hence, the design of a larger 41-cm long four-fin vehicle was initiated. The fore-aft symmetry of the four-fin design enables hover and higher precision positioning capabilities by decoupling vehicle pitch and heave control.

Computational fluid dynamics (CFD) studies helped minimize drag the vehicle hull geometry and determine optimal spacing between the front and back fins. Figure 2 shows the design layout of the four-fin vehicle.

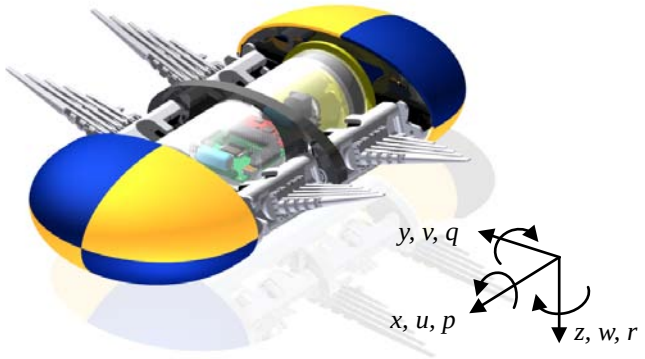

Fig. 2: Four-fin vehicle design with outer shell removed.

The four-fin vehicle design employs a water-tight cylinder for housing the battery, inertial force sensors, and control electronics. The flooded nose and tail sections, which contain high density foam for buoyancy trimming, house supplemental sensors. As with the two-fin vehicle, hardware control and all computation are performed by a 16 MHz ATmega2560 microcontroller.

Vehicle Model

The rigid-body vehicle hull is modeled separately from the elastic bending and twisting of the fins. The six degree-of-freedom (6-DOF) translational and rotational equations of motion for a rigid body are given in [16] as,

$$m\left(\left(\frac{\partial \vec{v}_0}{\partial t}\right)_r + \vec{\omega}\times\vec{v}_0 + \dot{\vec{\omega}}\times\vec{r}_G + \vec{\omega}\times\left(\vec{\omega}\times\vec{r}_G\right)\right) = \vec{f}_0$$
$$\tilde{I}_0\dot{\vec{\omega}} + \vec{\omega}\times\left(\tilde{I}_0\vec{\omega}\right) + m\vec{r}_G\times\left(\left(\frac{\partial \vec{v}_0}{\partial t}\right)_r + \vec{\omega}\times\vec{v}_0\right) = \vec{m}_0 \quad (1)$$

where $\boldsymbol{v_0} = [u\ v\ w]^T$ is the velocity vector, $\boldsymbol{\omega} = [p\ q\ r]^T$ is the angular rate vector, $\boldsymbol{r_G} = [x_G\ y_G\ z_G]^T$ is the center of gravity position vector, $\boldsymbol{I_0}$ is the inertia tensor, $\boldsymbol{f_0} = [X\ Y\ Z]^T$ is the external force vector, and $\boldsymbol{m_0} = [K\ M\ N]^T$ is the external moment vector. These vectors are computed with respect to the vehicle body-fixed frame as illustrated in Figure 2. The following mass properties were calculated based on CAD models and physical measurements of the four-fin vehicle.

$m = 2.95$ kg
$I_0 = [0.00750\ ,\ 0.0483\ ,\ 0.0442]$ N-m^2
$r_G = [0.0\ ,\ 0.0\ ,\ 1.1]$ cm

Equation (1) can be rewritten in matrix form as,

$$M\dot{\vec{v}} + C(\vec{v})\vec{v} + D(\vec{v})\vec{v} + \vec{g}(\vec{\eta}) = \vec{\tau} \qquad (2)$$

Here M is a matrix of rigid body mass and inertial terms, C is a matrix of centripetal and Coriolis terms, D is a matrix of hydrodynamic lift and drag terms, $\boldsymbol{g}$ is a vector of hydrostatic terms, $\boldsymbol{\nu} = [\boldsymbol{v_0}^T \ \boldsymbol{\omega}^T]^T$, $\boldsymbol{\eta} = [x \ y \ z \ \phi \ \theta \ \psi]^T$ is the position and orientation vector in the earth-fixed frame where ϕ, θ, and ψ are roll, yaw, and pitch angles, and $\boldsymbol{\tau}$ is a vector of all forces and moments external to the rigid body.

The characterization of the vehicle force and moment coefficients, used to populate the matrices in (2), follows the same computational process as we previously employed for the two-fin vehicle [12][13]. This process included determining hydrodynamic coefficients from vehicle geometry and CFD simulation, and hydrostatic coefficients from mass and buoyancy measurements. The resulting lift and drag coefficients, C_D and C_L, of the four-fin hull at selected angles of attack, α, as determined in CFD, are shown in Figure 3.

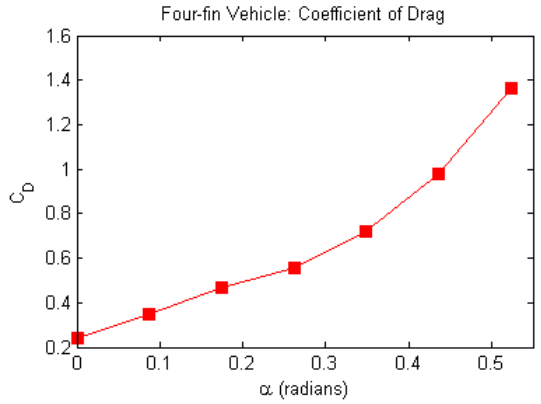

(a)

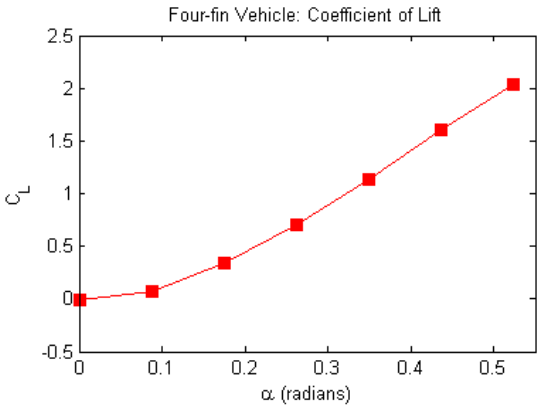

(b)

Fig. 3: (a) Vehicle drag and (b) vehicle lift coefficients computed for the four-fin vehicle at selected fixed angles of attack.

Fin Model

Fin placement and orientation on the vehicle are such that fin thrust forces act along the body x-axis, and lift forces act along the body z-axis. This decouples the thrust and lift components of force generated by the fins for the purposes of simplified modeling and control design. The vector of forces and moments acting on the vehicle body, $\boldsymbol{\tau}$, consists of both fin components and external disturbance components as written in (3). We then define $\boldsymbol{\tau}_{\mathbf{fins}}$ in (4) in terms of thrust and lift components of force from each of the four fins.

$$\vec{\tau} = \vec{\tau}_{fins} + \vec{\tau}_{external} \qquad (3)$$

$$\vec{\tau}_{fins} = \begin{bmatrix} f_{T,LF} + f_{T,LB} + f_{T,RF} + f_{T,RB} \\ 0 \\ -f_{L,LF} - f_{L,LB} - f_{L,RF} - f_{L,RB} \\ -y_L\left(f_{L,LF} + f_{L,LB}\right) - y_R\left(f_{L,RF} + f_{L,RB}\right) \\ x_F\left(f_{L,LF} + f_{L,RF}\right) + x_B\left(f_{L,LB} + f_{L,RB}\right) \\ -y_L\left(f_{T,LF} + f_{T,LB}\right) - y_R\left(f_{T,RF} + f_{T,RB}\right) \end{bmatrix} \qquad (4)$$

Here f_T is fin thrust, and f_L is fin lift. Subscripts 'LF', 'LB', 'RF', and 'RB' identify the left front, left back, right front, and right back fins, respectively. The x-position of the center of pressure on the fins is denoted by x_F for the front fins and x_B for the back fins. The y-position of the center of pressure on the fins is denoted by y_L for the left fins and y_R for the right fins. The center of pressure defines the location of the fin generated forces which is needed to compute the fin generated moments, and was determined using CFD as described in [17].

FIN FORCE CHARACTERIZATION

In order to populate the vector in (4), the forces generated by the fins are characterized as a function of various controllable fin stroke parameters as well as uncontrollable external interactions with the water and other fins. To determine the effects of these variables, fin-generated forces are measured and computed as described in the following sections. All experimental force measurements are taken of a single submerged fin mounted on a test apparatus described by Palmisano et al [17]. All force computations are made using the 3-D unsteady CFD code, FEFLO, described by Ramamurti et al [15].

Effect of Fin Control Parameters on Force Production

Results of CFD computations [15] and experimental tests characterize how changes in fin stroke amplitude, frequency, bias angle, and curvature affect the thrust and lift forces at zero free stream flow speed. A fin 'gait' is defined by the curvature time-history created by actuating the individual ribs in the fin. These gaits are then identified by the direction of force they are designed for such as 'forward' or 'reverse'.

Characterizing the effects of changing fin curvature and stroke amplitude on thrust from CFD data showed that increasing these parameters increases thrust generation [15]. However, since both stroke amplitude and flapping frequency are limited mechanically, optimal combinations of amplitude and frequency are experimentally found for high thrust and lift fin gaits (Figure 4). The best mix of these parameters for our vehicle was determined to be 100° and 1.82 Hz which yielded not only high force output, but also relatively low power consumption. These findings allowed us to fix amplitude and frequency as constants and to focus on fin curvature as the primary thrust control parameter.

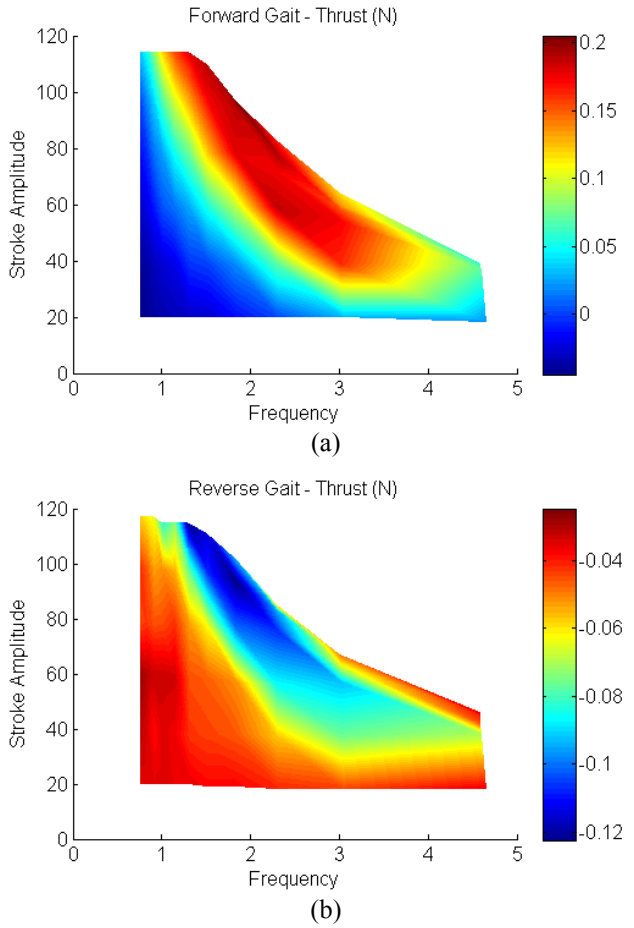

Fig. 4: Thrust in (a) forward and (b) reverse gaits as a function of frequency and bulk rotation angle. Red indicates maximum forward thrust, and blue indicates maximum reverse thrust.

Further, biasing the fin stroke up or down, as in Figure 5, affects fin lift generation while maintaining constant thrust [13]. The absence of any change in forward thrust is evidenced by the fact that forward thrust is generated along the fin axis of revolution by definition, and this axis is always parallel to the vehicle body *x*-axis regardless of the fin stroke bias. The up/down bias induces lift on the vehicle due to a span-wise component of force generated by the fins. The maximum bias allowed is a function of the fin stroke amplitude and the mechanical limits on fin stroke angle.

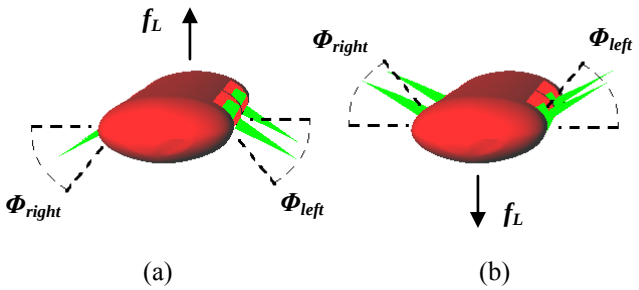

Fig. 5: Vehicle images showing all four fins with strokes (a) biased down to produce positive lift and (b) biased up to produce negative lift.

While keeping flapping frequency and amplitude fixed, fin thrust can be varied by using weighted combinations of a reverse gait and forward gait (each with distinct curvature time-histories) [17]. Combinations of these gaits, as shown in Figure 6, have little effect on fin lift. As shown in Figure 7, fin lift can be varied though biasing the fin mean stroke amplitude, a parameter which has a negligible effect on fin thrust.

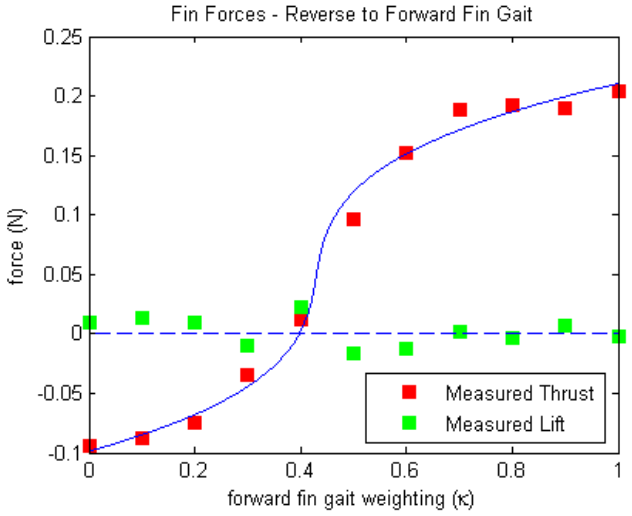

Fig. 6: A curve fit (see (5)) of experimental thrust data for a single isolated fin at zero free stream flow velocity as the fin gait is shifted from full reverse kinematics ($\kappa = 0.0$) to full forward kinematics ($\kappa = 1.0$).

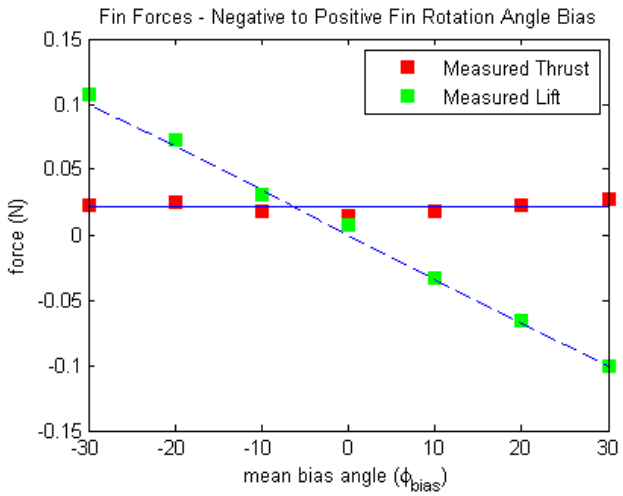

Fig. 7: A curve fit (see (6)) of experimental lift data for a single isolated fin at zero free stream flow velocity as the fin rotation angle bias is shifted from Φ_{bias} = -30° to Φ_{bias} = 30°. Fin gait weighting is set at κ = 0.4 for constant near zero thrust.

The experimental thrust and lift in Figures 6 and 7 were measured in zero free stream flow. For these sets of data, an exponential function of forward-reverse gait weighting was chosen as a best fit for fin thrust (5), and a linear function of mean stroke angle bias was chosen as a best fit for fin lift in the range of our operating parameters (6). The equations for estimating thrust and lift are given as,

$$f_{T,\kappa} = \frac{-2.4}{8.0 - 0.10 \cdot e^{10 \cdot \kappa}} + 0.20 \tag{5}$$

$$f_{L,\Phi_{bias}} = -0.0033 \cdot \Phi_{bias} \tag{6}$$

Here κ is the weighting of the fin gait, defining the transition from full reverse gait to full forward gait. It ranges from zero to one with zero being 100% reverse kinematics and one being 100% forward kinematics (0.5 is a rigid fin with no curvature). The term, Φ_{bias}, is the mean stroke angle bias of the fin from a horizontal position (fin ribs pointing along the body y-axis).

Effect of Free Stream Velocity on Force Production

The free stream inflow velocity must also be accounted for in the models of fin force production. As the incoming flow speed increases, the forces generated by the fin are altered, most notably with a decrease in thrust. Using the forward gait, the thrust output by a single isolated fin is plotted against free stream velocity for the range of operating speeds we have tested in Figure 8.

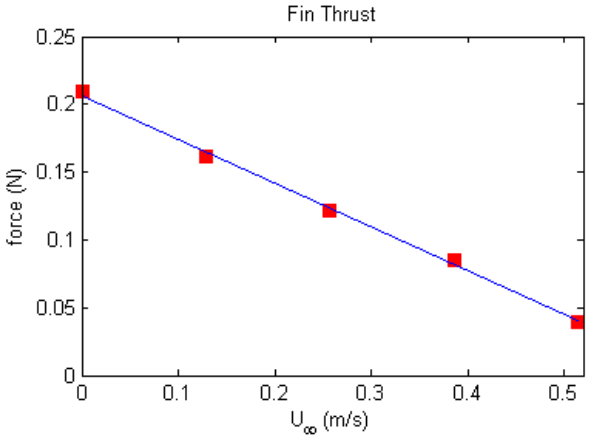

Fig. 8: CFD computed data showing thrust for a single isolated fin as a function of incoming flow velocity.

In studies of propellers and flapping wings, a relationship between thrust coefficient and advance ratio has commonly been presented [18][19][20] where advance ratio is defined as the free stream flow into the propeller or flapping mechanism divided by the average tip speed [21]. Our average fin tip speed using the forward gait is calculated as,

$$\begin{aligned} V_{fin,tip} &= 2\Phi_{bulk} Rf \\ &= 2.897 \frac{rad}{cycle} \cdot 1.82 \frac{cycles}{s} \cdot 0.102m \\ &= 0.538 \frac{m}{s} \end{aligned} \tag{7}$$

where Φ_{bulk} is the amplitude of the fin stroke, R is the distance from rotation axis to fin tip, and f is the frequency of the fin stroke. At this fin tip speed, the advance ratio for our fin is between zero and 0.96 for the range of operating speeds we have tested. In this range of advance ratios, thrust follows a decreasing linear relationship with free stream speed in both propeller and flapping wing studies [18][19][20], and this is what we have observed for our fin using the forward gait. We have modeled this relationship between free stream speed and thrust for one of our single isolated fins from the data in Figure 8 as,

$$\Delta f_{T,U_\infty} = -0.330 \cdot U_\infty \tag{8}$$

where $\Delta f_{T,U\infty}$ is the change in thrust due to incoming flow, and U_∞ is the incoming free stream velocity. However, this linear relationship has only proven valid for the forward gait, which uses a symmetric stroke and curvature to produce forward thrust. More analysis is required to better explain the relationship between free stream velocity and thrust across a

greater range of fin parameters and that is beyond the scope of this paper.

Effect of Leading-Trailing Fin Interaction on Force Production

For a four-fin vehicle with two fins in-line on both the right and left sides, consideration must be made for the hydrodynamic effects of fin flapping on the other fins' force production. These effects are studied in CFD focusing on the interaction between front and back fin sets using a 100% forward gait (κ = 1.0) for all fins. The following results are based on our vehicle design with a separation distance from trailing edge of the front fin to leading edge of the back fin of 0.05 m. The impact of the fluid motion generated by an individual fin on other fins is relatively insignificant in a vehicle hover condition at zero free stream flow velocity as shown in Figure 9. However, even at slow forward speeds, the output wake of the front (leading) fins impacts the force generation of the back (trailing) fins due to a wake capture effect. A summary of the thrust and lift results for a vehicle traveling at 0.514 m/s (one knot) is shown in Figure 10 where a negative phase indicates the back fin rotational position is behind the front fin and positive phase indicates the back fin rotational position is ahead of the front fin.

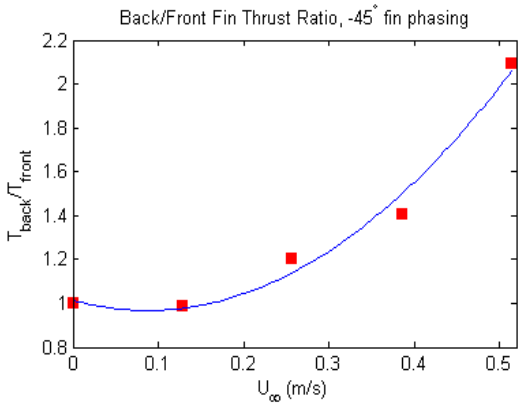

Fig. 9: CFD computed data showing the improvement in back fin thrust over front fin thrust at a -45° back fin phase lag.

At a forward speed of 0.514 m/s (one knot), the thrust generated by the back fins is more than twice that generated by the front fins when phasing the back fins at -45° (12.5% of the stroke time). Even without phasing the fins to optimize the back fin thrust, there is still an 80% increase in thrust generation for the back fins compared with the front fins. However, lift generation remains mostly unaffected, a beneficial finding as no unwanted pitch moment is created when using the forward gait. Similar results are found at a forward speed of 0.257 m/s (0.5 knots), and a simple quadratic model was fit to the ratio between back fin and front fin thrust generation as a function of forward speed as shown in Figure 9.

The quadratic function used to fit the data in Figure 9 is given by,

$$\frac{f_{T,B}}{f_{T,F}} = g(U_\infty) = 5.995 \cdot U_\infty{}^2 - 1.053 \cdot U_\infty + 1.014 \qquad (9)$$

This equation can be arranged to give rear fin thrust as a function of both free stream velocity and front fin thrust.

$$f_{T,B} = g(U_\infty) \cdot f_{T,F} \qquad (10)$$

This function describing the leading-trailing fin effect is applied to our fin thrust models within our four-fin vehicle dynamics model.

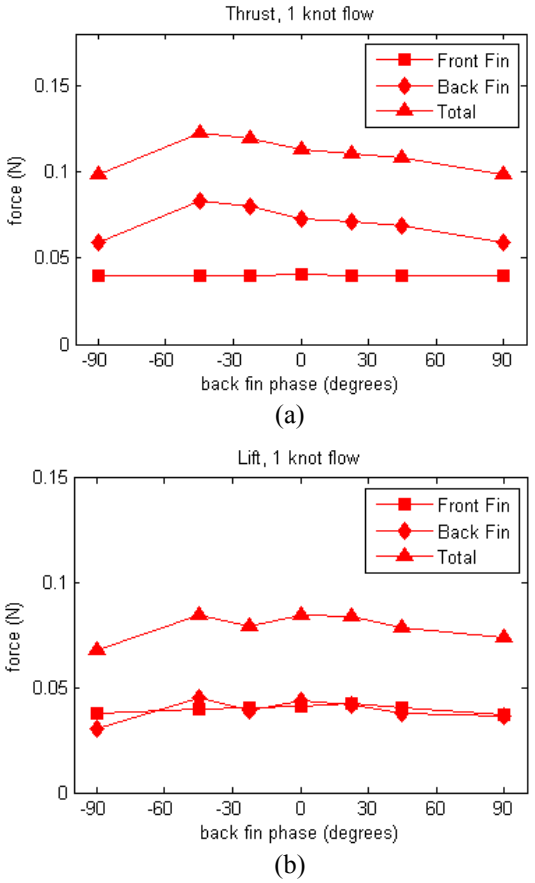

Fig. 10: (a) Thrust and (b) lift generated by front fin and back fin. At one knot flow, the vortices off the front fin give a boost to the thrust of the back fin for our particular configuration.

Fin Force Models

Combining the effects on fin force generation due to control parameter variation, leading-trailing fin interaction, and free stream flow velocity gives us a high fidelity model of fin

force generation on the four-fin vehicle. Equation (11) represents the full model including these effects.

$$
\begin{aligned}
f_{T,F} &= f_{T,\kappa} + \Delta f_{T,U_\infty} \\
f_{T,B} &= g\left(U_\infty\right)\cdot\left(f_{T,\kappa} + \Delta f_{T,U_\infty}\right) \\
f_{L,F} &= f_{L,\Phi_{bias}} \\
f_{L,B} &= f_{L,\Phi_{bias}}
\end{aligned}
\tag{11}
$$

Here the subscripts 'F' and 'B' identify front and back fins. Now that fin forces are output as functions of curvature, stroke angle bias, fin-fin interaction, and free stream velocity, we utilize this model to map vehicle controller outputs to the fin forces represented as part of the vehicle model given in (3).

CONTROL METHODS

In previous work we evaluated the benefits of two control methods [13]. The first method, called weighted gait combination (WGC), used combinations of thrust-generating and lift-generating fin gaits to produce vectored propulsive forces. The second method, called mean bulk angle bias (MBAB), used weighted forward-reverse gait control with stroke bias angle control. Between these two control methods, our results showed that MBAB better decoupled control over body-fixed thrust and lift forces, and yielded better vehicle response characteristics in simulation. As such, the MBAB method is used to control the four-fin vehicle.

Fin Kinematics Control

Flapping the fins symmetrically about the body *xy*-plane, a stroke-averaged zero lift is produced. This symmetry is attained by controlling the forward-reverse gait weighting of the fins to affect changes in thrust resulting in near-zero lift generation as shown in Figure 6. This is beneficial for restricting vehicle motion to a horizontal plane. As we have mostly decoupled control over thrust and lift forces, we can rewrite (4) as,

$$
\vec{\tau}_{fins} = B\vec{u}
$$

$$
B = \begin{bmatrix}
1 & 1 & 1 & 1 & 0 & 0 & 0 & 0 \\
0 & 0 & 0 & 0 & 0 & 0 & 0 & 0 \\
0 & 0 & 0 & 0 & -1 & -1 & -1 & -1 \\
0 & 0 & 0 & 0 & -y_L & -y_L & -y_R & -y_R \\
0 & 0 & 0 & 0 & x_F & x_B & x_F & x_B \\
-y_L & -y_L & -y_R & -y_R & 0 & 0 & 0 & 0
\end{bmatrix}
\tag{12}
$$

$$
\vec{u} = \begin{bmatrix} f_{T,LF} & f_{T,LB} & f_{T,RF} & f_{T,RB} & \cdots \\ f_{L,LF} & f_{L,LB} & f_{L,RF} & f_{L,RB} \end{bmatrix}^T
$$

We then use the fin model characterized in section III to map kinematics commands to the force outputs in ***u***. The PID control laws used to command fin kinematics changes must also be tuned to output the desired forces for various maneuvers. Taking the inverse of the equations for fin forces, (5) and (6), we are able to map desired thrust and lift to desired kinematics for zero free stream flow velocity for the leading fins, as shown in (13).

$$
\begin{aligned}
\kappa_c &= \frac{1}{10}\ln\left(\left(\frac{-24}{f_{T,c} - 0.2}\right) - 80\right) \\
\Phi_{bias,c} &= -303 \cdot f_{L,c}
\end{aligned}
\tag{13}
$$

Here κ_c is commanded forward-reverse fin gait weighting, and $\Phi_{bias,c}$ is commanded fin mean rotation angle bias. The minimum and maximum values for these parameters are limited by the mechanical constraints on fin curvature and stroke angle. Further, in certain maneuvers we must place artificial limits on the fin kinematics. For example, to achieve a heading change in hover (without translation in the xy-plane) the left and right fins must produce equal and opposite thrust vectors. Since full reverse kinematics produce -0.1N of thrust (Figure 6), the forward kinematics must be limited to producing +0.1N of thrust to achieve a heading change in hover. We see in Figure 11 that this sets an artificial maximum on the commanded gait weighting of $\kappa_c = 0.51$ for this maneuver.

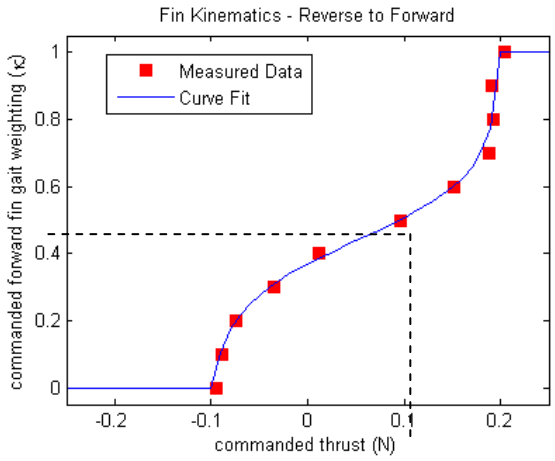

Fig. 11: A curve fit of experimental thrust data for a single isolated fin showing the necessary fin gait weighting as commanded thrust changes for each fin at zero free stream flow velocity.

The data in Figure 11 assume zero forward speed, and can be shifted to account for both the free stream flow velocity and leading-trailing fin interactions as outlined in the Fin Force Characterization section.

Vehicle Control Architecture

Adjustments were made to the MBAB controller gains designed for the two-fin vehicle [13], but the architecture remains the same. Vehicle errors in surge motion (x-axis translation) dictate commands for fin thrust changes to all fins. Errors in heave motion (z-axis translation) dictate commands for fin lift changes to all fins. Errors in roll motion (x-axis rotation) dictate commands for differential lift changes between left and right fins. Errors in pitch motion (y-axis rotation) dictate commands for differential lift changes in forward and back fins. Errors in yaw motion (z-axis rotation) dictate commands for differential thrust changes in left and right fins. The vehicle has no direct control over sway motion (y-axis translation), and instead commands yaw motion changes to move in this direction. The direction of yaw motion depends on the sway error and the vehicles forward velocity as represented in (14).

$$f_{T,LF,c} = -\mathrm{sgn}(u)\cdot\left(K_{y,p}\cdot y_e + K_{y,d}\cdot \dot{y}_e\right)$$
$$f_{T,RF,c} = \mathrm{sgn}(u)\cdot\left(K_{y,p}\cdot y_e + K_{y,d}\cdot \dot{y}_e\right) \quad (14)$$

Here $K_{y,p}$ is the proportional gain and $K_{y,d}$ is the derivative gain on *y*-position, and y_e is the *y*-position error. We see from the sign function, *sgn()*, that if the vehicle is moving forward the command is to turn one way, and if the vehicle is moving reverse the command is to turn the other way.

The following results are for a four-fin vehicle using the MBAB method of control from [13] with the change to sway control as outlined in (14).

VEHICLE CONTROL RESULTS

Open Loop Results and Model Validation

Initial experimental results of the four-fin vehicle were conducted to begin validation of the vehicle dynamics model and to assess various performance metrics. These metrics include forward and reverse speed capability, turn radius, and rotational speed.

The top forward velocity was first assessed using interpolation of CFD data (Figure 12), and using response data from open-loop control simulation in MATLAB (Figure 13). The responses were compared to validate the vehicle modeling process.

As expected, we see in Figure 13 the four-fin vehicle attained a higher top speed (0.42 m/s or 0.81 knots) than the two-fin vehicle (0.34 m/s or 0.66 knots). However, it is only marginally higher as the drag on the larger body of the four-fin vehicle negates some of the thrust gained from doubling the number of fins. The top speed observed in MATLAB simulation was validated by CFD data showing a top speed of 0.41 m/s (0.79 knots), a 2.5% difference, where thrust and drag intersect in Figure 12.

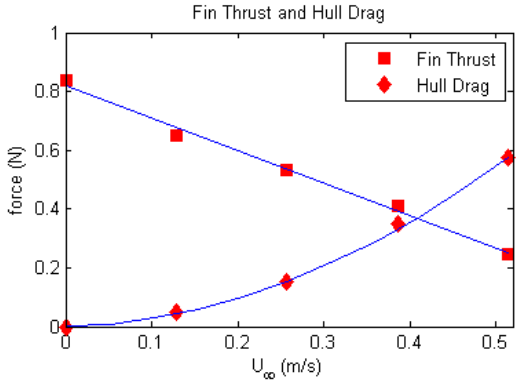

Fig. 12: CFD computed fin thrust and hull drag. The fitted data curves show the intersection where vehicle maximum forward velocity is reached.

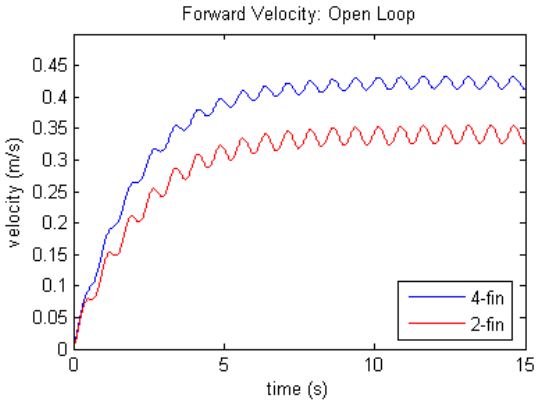

Fig. 13: Comparison of forward speeds of the two-fin and four-fin vehicles in simulation. The four-fin vehicle achieved 0.42 m/s whereas the two-fin vehicle achieved 0.34 m/s.

The only experimental measurement taken for vehicle speed was a time-averaged velocity. The vehicle traveled forward from rest to two meters using full forward thrust kinematics (κ = 1.0) for all four fins in 8.23 seconds – a time averaged velocity of 0.24 m/s (0.47 knots). From the results in Figure 13, we computed the average velocity of the model in simulation after traveling 2 meters as 0.25 m/s (0.49 knots), a difference of 4.1%. In addition to measuring the average velocity, the vehicle thrust was measured at zero free stream flow using a spring scale with the fins flapping at 100% forward gait. The experimental thrust using this relatively imprecise measurement had a time averaged value of ~0.8 N which matches the value for thrust computed in CFD (Figure 12).

An open loop test was also conducted to characterize vehicle heading angle response, and again to compare model simulation performance with experimental performance. The right fins were set at full reverse kinematics (κ_R = 0.0) and the left fins were set to closely match the opposite thrust of the right fins as determined in Figure 11 (κ_L = 0.5). At *t* = 11s the gait

weighting inputs were reversed (κ_L = 0.0, κ_R = 0.5). The simulated and experimental responses show very good agreement (Figure 14) with a 30°/s maximum turning rate, 4s time from zero to maximum speed, and braking angle of 35° – the amount of residual turning distance after fin kinematics are reversed.

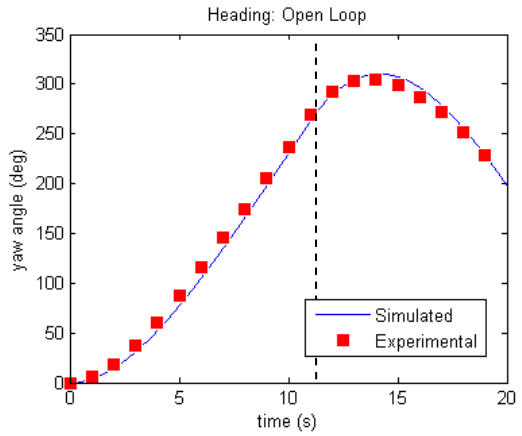

Fig. 14: Comparison of experimental and simulated open-loop heading angle responses.

Closed Loop – Autonomous Heading

After validating the four-fin vehicle model, and implementing state feedback control, initial closed-loop experiments were done to test heading angle control. In Figure 15, a comparison of experimental and simulated results is given for a simple proportional control algorithm. The blue curve represents the computed heading in simulation from the output of the modeled sensors. We see the results match well with a 30°-40° amplitude and 6.5s period.

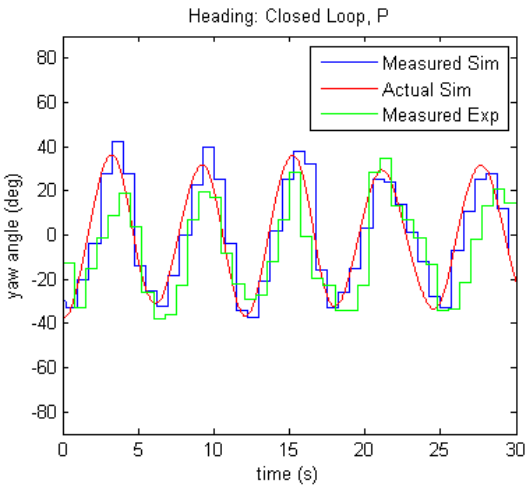

Fig. 15: Comparison of experimental and simulated closed-loop heading angle responses with proportional control.

The comparison in Figure 15 has further validated our model by showing that the frequency and amplitude of the undamped response in vehicle heading attitude matches that of the actual vehicle as given by onboard sensor measurements.

The results of this initial closed loop heading test reiterate the need for an improved controller to dampen the highly oscillatory responses. The addition of a derivative term to the control algorithms enables a more precise, less oscillatory heading angle response, as shown in Figure 16. Experiments with the actual vehicle also benefitted from the addition of a small integral term to eliminate heading angle errors caused by thrust production differences between fins. A step change of 180° in heading command with the PID controller implemented yields a nearly critically damped response rise time of ~7 seconds.

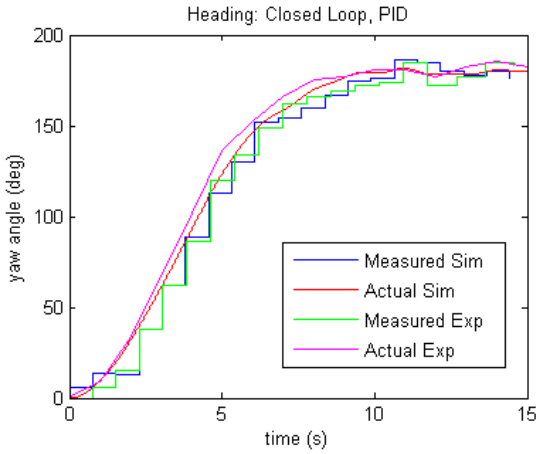

Fig. 16: Comparison of experimental and simulated closed-loop responses to a step change of 180° in heading with PID control.

DISCUSSION AND CONCLUSIONS

A robust model of flapping fin force generation has been created to discern the effects of fin curvature, stroke amplitude, stroke bias, leading-trailing fin wake capture effects from stroke phasing, and free stream flow velocity. A 6-DOF system model was derived for a four-fin vehicle and has been validated through comparison of simulation results with experimental results. Using the same principles for vehicle modeling and controller design as we had for our two-fin vehicle, desirable PID gains for flapping fin kinematics control were chosen to produce the fin forces required for precise maneuvering of this four-fin vehicle.

Our current research involves incorporating sensors to measure the environment around the vehicle. This work will enable expanded vehicle mission capabilities utilizing acoustic sensors to detect obstacles and cameras to document the underwater environment. Higher level control capability will be studied including waypoint navigation and object avoidance.

ACKNOWLEDGMENTS

Acknowledgments to the Office of Naval Research and the Naval Research Laboratory Base Program for supplied support.

REFERENCES

[1] J. E. Colgate and K. M. Lynch, "Mechanics and Control of Swimming: A Review," *IEEE Journal of Oceanic Engineering*, vol. 29, pp. 660-673, July 2004.

[2] R. W. Blake, "The mechanics of labriform motion I. Labriform locomotion in the angelfish (*pterophyllum eimekei*): An analysis of the power stroke", J*ournal of Experimental Biology*, vol. 82, 1979, pp. 255-271.

[3] N. Kato, "Hydrodynamic Characteristics of a Mechanical Pectoral Fin", *Journal of Fluids Engineering, Transactions of the ASME*, vol. 121, pp. 605-613, 1999.

[4] N. Kato, "Control Performance of a Fish Robot with Mechanical Pectoral Fins in the Horizontal Plane", *Journal of Oceanic Engineering, Transactions of the IEEE*, vol. 25, no. 1, 2000.

[5] B. Hobson, M. Murray, and C. A. Pell, "PilotFish: Maximizing Agility in an Unmanned-Underwater Vehicle", *Proceedings of the International Symposium on Unmanned Untethered Submersible Technology*, Durham, NH, 1999.

[6] S. Licht, V. Polidoro, M. Flores, F. S. Hover, and M. S. Triantafyllou, "Design and Projected Performance of a Flapping Foil AUV", *IEEE Journal of Oceanic Engineering*, vol. 29, no. 3, 2004.

[7] Y. Ando, N. Kato, H. Suzuki, T. Ariyoshi, K. Suzumori, T. Kanda, and S. Endo, "Elastic Pectoral Fin Actuators for Biomimetic Underwater Vehicles", *Proceedings of the 16th International Offshore and Polar Engineering* Conference, pp. 260-267, 2006.

[8] J. Palmisano, R. Ramamurti, K.J. Lu, J. Cohen, W. C. Sandberg, and B. Ratna, "Design of a Biomimetic Controlled-Curvature Robotic Pectoral Fin", *2007 IEEE Int. Conf. on Robotics and Automation*, Roma, Italy.

[9] K. W. Moored, W. Smith, W. Chang, and H. Bart-Smith, "Investigating the thrust production of a myliobatoid-inspired oscillating wing", *3rd International CIMTEC Conference*, Acireale, Italy, June 8-13, 2008.

[10] R. Ramamurti and W. C. Sandberg, "Computational Fluid Dynamics Study for Optimization of a Fin Design", *24th AIAA Applied Aerodynamics Conference*, AIAA-2006-3658, 2006.

[11] M. Bozkurttas, H. Dong, R. Mittal, P. Madden, and G. V. Lauder, "Hydrodynamic Performance of Deformable Fish Fins and Flapping Foils", AIAA 2006-1392, 2006.

[12] J. Geder, J. Palmisano, R. Ramamurti, W. C. Sandberg, and B. Ratna, "A New Hybrid Approach to Dynamic Modeling and Control Design for a Pectoral Fin Propelled UUV", *15th International Symposium on Unmanned Untethered Submersible Technology*, Durham, New Hampshire, USA, August 19-22, 2007.

[13] J. Geder, J. Palmisano, R. Ramamurti, W. C. Sandberg, and B. Ratna, "Fuzzy Logic PID Based Control Design and Performance for Pectoral Fin Propelled Unmanned Underwater Vehicle", *International Conference on Control, Automation, and Systems*, Seoul, Korea, October 14-17, 2008.

[14] J. Geder, R. Ramamurti, J. Palmisano, M. Pruessner, B. Ratna, and W. C. Sandberg, "Sensor Data Fusion and Submerged Test Results of a Pectoral Fin Propelled UUV", *16th International Symposium on Unmanned Untethered Submersible Technology*, Durham, New Hampshire, USA, August 23-26, 2009.

[15] R. Ramamurti, J. D. Geder, J. Palmisano, B. Ratna, and W. C. Sandberg, "Computations of Flapping Flow Propulsion for Unmanned Underwater Vehicle Design", *AIAA Journal*, vol. 48, no. 1, pp. 188-201, January 2010.

[16] T. I. Fossen, *Guidance and Control of Ocean Vehicles*, New York, John Wiley & Sons, 1994.

[17] J. S. Palmisano, J. D. Geder, R. Ramamurti, M. Pruessner, W. C. Sandberg, and B. Ratna, "Robotic Pectoral Fin Thrust Vectoring Using Weighted Gait Combinations", submitted for publication in *Applied Bionics and Biomechanics*, November 2010.

[18] E. P. Warner, *Airplane Design: Performance*, York, PA, McGraw-Hill Book Company, Inc., 1936, pp. 467-471.

[19] E. M. Lewandowski, *The Dynamics of Marine Craft: Maneuvering and Seakeeping*, Singapore, World Scientific Publishing, 2004, pp. 83-86.

[20] H. Nagai, K. Isogai, and T. Hayase, "Measurement of Unsteady Aerodynamic Forces of 3D Flapping Wing in Hovering to Forward Flight", *26th International Congress of the Aeronautical Sciences*, Anchorage, Alaska, USA, September 14-19, 2008.

[21] J. A. Walker, "Functional Morphology and Virtual Models: Physical Constraints on the Design of Oscillating Wing, Fins, Legs, and Feet at Intermediate Reynolds Numbers", *Integrative and Computational Biology*, vol. 42, pp. 232-242, 2002.